Journal of Materials Chemistry A

PAPER

View Article Online
View Journal | View Issue

Cite this: J. Mater. Chem. A, 2017, 5, 25056

rGO/SnS_2/TiO_2 heterostructured composite with dual-confinement for enhanced lithium-ion storage†

Hong-En Wang,[abc] Xu Zhao,[b] Xuecheng Li,[a] Zhenyu Wang,[d] Chaofeng Liu,[b] Zhouguang Lu,*[d] Wenjun Zhang*[c] and Guozhong Cao*[b]

Received 29th September 2017
Accepted 10th November 2017

DOI: 10.1039/c7ta08616d

rsc.li/materials-a

Next-generation lithium ion batteries (LIBs) require new electrode materials with high energy/power density, good safety and long cycle life. SnS_2 is a promising anode candidate due to its high theoretical capacity; however, it still suffers from low electronic/ionic conductivity and large volume expansion during lithiation, which hinder its practical application. Herein, we report the construction of a two-dimensional (2D) heterojunction composite electrode comprised of ultrafine SnS_2 and TiO_2 nanoparticles deposited on reduced graphene oxide (rGO) nanosheets. This composite exhibits superior lithium-ion storage capability in terms of high capacity, superior rate property and excellent cycling stability. The performance improvement is primarily due to the synergic coupling of various components in the composite: (1) rGO serves as a fast channel for rapid electron transport and an ideal host for the mass loading of SnO_2 and TiO_2; (2) ultrafine SnS_2 nanoparticles with abundant defects manifest high reactivity for lithiation; and (3) TiO_2 forms intimate contact with SnS_2, boosting Li^+/e^- transfer at the interfaces. TiO_2 also effectively pins the SnS_2 particles, which prevents their migration, aggregation and detachment from the rGO substrate, ensuring the structural integrity and cycling stability of the composite electrode. The dual-confinement strategy using N–Sn bonds and TiO_2 decoration together with heterostructure construction presented herein can pave the way for the development of more advanced composite materials for high-performance alkali-metal ion batteries.

Introduction

Lithium ion batteries (LIBs) with high energy and power density are urgently required for emerging applications in electric vehicles, smart grids and storage of electricity from renewables.[1] Therefore, new electrode materials are highly desired to afford higher specific capacities, better safety and minimum environmental impact. Currently, commercial graphite can hardly satisfy the increased requirements of anodes due to its low capacity, poor rate capability and inferior safety. Various anode candidates based on intercalation,[2,3] alloys,[4] and conversion reactions,[5,6] or their combination,[7] have been intensively investigated as anode candidates for high-performance LIBs. Among them, metallic tin[8] and tin oxides (SnO_2 (ref. 7 and 9) and SnO[10]) and sulfides (SnS_2 (ref. 11) and SnS[12,13]) have attracted much attention due to their high theoretical capacity, low cost, and environmental friendliness. In particular, SnS_2 shows great promise as an anode for Li/Na-ion batteries compared to SnO_2 due to its increased intrinsic electrical conductivity. In addition, cleavage of Sn–S bonds is easier than that of Sn–O bonds, leading to the enhanced redox reversibility of SnS_2. Unfortunately, SnS_2 still suffers from large volume change and sluggish Li^+ diffusion during (de)lithiation, leading to the deterioration of cyclability and poor rate property.[14]

One effective approach to enhance the electrochemical reactivity of SnS_2 is to reduce its particle size to the nanoscale. As the particle size decreases, not only is Li^+ transfer much easier due to the shortened diffusion length but also the strain of volume expansion associated with Li^+ intercalation can be better accommodated. Various low-dimensional nanostructures have been intensively synthesized to enhance the redox kinetics of SnS_2, such as nanoparticles,[15] nanobelts,[16] nanoribbons,[17] nanosheets/nanoplates,[18,19] and porous 3D nanoarchitectures.[20] However, low-dimensional nanostructures easily aggregate during synthesis and electrochemical cycling, leading to

[a]State Key Laboratory of Advanced Technology for Materials Synthesis and Processing, Wuhan University of Technology, Wuhan, China

[b]Department of Materials Science and Engineering, University of Washington, Seattle, WA, USA. E-mail: gzcao@u.washington.edu

[c]Department of Materials Science and Engineering, Center of Super Diamond and Advanced Films (COSDAF), City University of Hong Kong, Hong Kong, China. E-mail: apwjzh@cityu.edu.hk

[d]Department of Materials Science and Engineering, Southern University of Science and Technology of China, Shenzhen, China. E-mail: luzg@sustc.edu.cn

† Electronic supplementary information (ESI) available: TGA, additional XPS, FTIR, SEM and galvanostatic charge–discharge curves. See DOI: 10.1039/c7ta08616d

inferior cycling stability. In addition, the increase in interfaces between the SnS_2 particles and electrolyte could promote the continuous formation of a thick solid-electrolyte interphase (SEI) layer during cycling.

Apart from nanostructuring, hybridization of SnS_2 with conductive species (*e.g.*, porous carbon matrices,[21] carbon nanotubes[22] and graphene[23]) can increase the electrical conduction of the active materials and reduce the electrochemical polarization during charge/discharge. Particularly, various reduced graphene oxide (rGO)/SnS_2 composites have been successfully designed to afford superior electrochemical Li/Na storage performances.[24,25] Such nanocomposites take full advantage of the good flexibility, strength, high electrical conductivity and surface area of rGO, as well as the nanostructured SnS_2 with enhanced reaction kinetics for Li^+ insertion. However, aggregation, inhomogeneous distribution and detachment of SnS_2 from rGO nanosheets remain a big challenge for long-term cycling. These issues are attributed to the weak interface interaction between the polar SnS_2 and nonpolar rGO, which becomes increasingly unstable during repeated lithiation/delithiation. Recently, strong chemical interaction has been introduced to better stabilize the SnS_2/rGO interface for longer cyclability. For example, Guo *et al.* reported that N-doped rGO/SnO_2 exhibits better lithium storage capability due to the formation of N–Sn chemical bonds at the SnO_2 and N-doped rGO interface.[26] Similarly, Xiong *et al.* reported that N-doped rGO/SnS_2 manifests improved cycling stability for Na^+ storage due to the presence of N–Sn chemical bonds.[27] In these reports, the enhanced N–Sn interaction is mainly induced by the electrostatic attraction between the electron-rich N atom and electron-depleted Sn^{4+} ions. However, such strategy still has some deficiencies: (i) the low N-doping content in the rGO lattice may lead to incomplete anchoring of all the SnS_2 nanoparticles at high mass loadings and (ii) the chemical N–Sn bonding strength gradually weakens during lithiation and very weak chemical interactions can be expected at interfaces between N-group and metallic Sn or Li_xSn alloys due to strong electrostatic repulsion. Thus, the discharge product Sn/Li_xSn can migrate and aggregate on the rGO basal plane, and eventually detach from the rGO nanosheets, leading to gradual capacity decay upon long-term cycling. Therefore, new strategies are necessary to solve this pertinent issue.

Compared to chemical anchoring, direct physical pinning offers an alternative way to stabilize SnS_2 on rGO. This method has recently been proven to improve the cycling performance of Si anodes with thin amorphous TiO_2 coating by Zhao's group.[28] Compared to inert inorganic coating (*e.g.*, Al_2O_3),[29] TiO_2 has several unique advantages. First, TiO_2 is a safe anode candidate for LIBs and it can be readily transformed into various nanostructures with versatile morphologies and pore structures,[2,3,30] which can contribute additional capacity. Second, a thin, conductive Li_xTiO_2 layer is formed during initial lithiation, facilitating rapid electronic/ionic transmission. Third, TiO_2 coating can change the composition of the SEI, and help form more stable SEI films with improved initial coulombic efficiency. Therefore, the rational construction SnS_2/TiO_2 nanocomposites with well-defined morphologies, compositions and interface structures can enhance the electrochemical properties of anodes.

Herein, we report the design and synthesis of a ternary rGO/SnS_2/TiO_2 nanosheet composite as an advanced anode for LIBs. In this composite, TiO_2 nanocrystals are mainly deposited on/nearby SnS_2 nanocrystals and bare rGO surface, instead of densely packed together given the fact that mesoporous TiO_2 spheres constructed from interconnected nanoparticles would be obtained in the absence of rGO/SnS_2.[31,32] The very small volume change (<4%) of TiO_2 upon lithiation and its nanocrystalline character enable stable cycling during charge/discharge without detachment from rGO. Furthermore, the TiO_2 decoration surrounding SnS_2 is expected to better regulate the separation and dispersion of SnS_2 and its discharge/(re)charge product, physically blocking possible aggregation during repeated electrochemical cycling. Furthermore, the less dense TiO_2 can accommodate the volume expansion/contraction of SnS_2 nanocrystals, relieving the accumulation of undesired stress/strain. This heterostructure electrode also exhibits superior electrochemical properties due to its unique structural characteristics: (i) the rGO nanosheets and defective SnS_2 nanoparticles afford rapid electron transport and rich active sites for Li^+ insertion/extraction with short diffusion paths; (ii) the TiO_2 capping layer prevents the migration, aggregation and detachment of SnS_2 during (de)lithiation, leading to enhanced cyclability; (iii) the engineered SnS_2/TiO_2 heterojunctions with a built-in electric field boost the Li^+/e^- transfer at their interfaces during the initial lithiation process; and (iv) the formation of conductive Li_xTiO_2 decreases the SnS_2/TiO_2 interface resistance and the active TiO_2 coating layer affords additional Li^+ storage capacity. The strategy proposed herein can potentially be extended to the design and interface engineering of a wide array of heterostructure composite electrodes for Li- and Na-ion batteries.

Experimental section

Material synthesis

Scheme 1 shows the overall synthetic procedure for the ternary rGO/SnS_2/TiO_2 composite. First, rGO/SnS_2 was prepared *via*

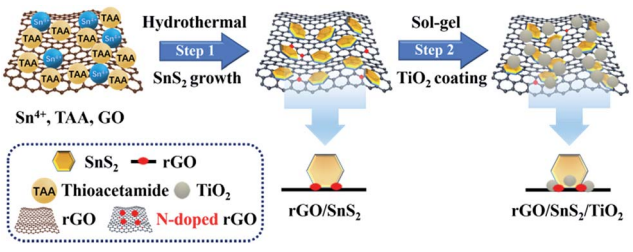

Scheme 1 Synthesis of rGO/SnS_2 and rGO/SnS_2/TiO_2 nanocomposites. In step 1, SnS_2 nanoparticles were grown on rGO nanosheets, and simultaneously graphene oxide (GO) was *in situ* reduced to rGO by ethylenediamine. The SnS_2 nanoparticles were tightly anchored on the rGO surface by the formation of C–S and N–Sn bonds at the rGO/SnS_2 interface. In step 2, TiO_2 nanoparticles were decorated on the SnS_2 nanoparticles, forming abundant junctions.

a solution process followed by freeze-drying according to a recent work[27] with some modifications. Typically, 60 mg graphene oxide (GO) powder was dispersed in 50 mL deionized (DI) water and further ultrasonicated for 0.5 h. Then 0.7 g $SnCl_4 \cdot 5H_2O$, 0.3 g thioacetamide (TAA) and 0.12 mL ethylenediamine (EDA) were dissolved in the GO aqueous solution under vigorous stirring. The resultant mixture was reacted in a sealed glass vessel at 95 °C for 12 h. During this solution process, Sn^{4+} ions were adsorbed on the negatively charged GO surface with rich $-COO^-$ groups *via* electrostatic interactions. Upon heating, the surface adsorbed Sn^{4+} ions reacted with the S^{2-} ions from TAA decomposition to form SnS_2 nuclei which then grew into nanocrystals on the GO substrate. Meantime, EDA could reduce GO into rGO, boosting its electrical conductivity. The resultant precipitates were harvested by centrifugation and washed with deionized water 3 times. Finally, the rGO/SnS_2 sample was freeze-dried for 3 days before collection.

Next, a titanium glycolate (TEG) precursor was coated on the rGO/SnS_2 surface by precipitation in an acetone bath with trace H_2O under stirring. In a typical procedure, the rGO/SnS_2 composite was dispersed in 100 mL acetone containing 0.5 mL deionized water with vigorous stirring, and then 20 mL ethylene glycol dissolved in 0.5 mL tetraisopropyl titanate was dropwise added to the acetone bath under vigorous stirring. The high surface area of the rGO/SnS_2 hybrid nanosheets ensured the uniform deposition of TEG surrounding the SnS_2 nanoparticles and on some bare rGO surface as well. Note that spherical TEG particles would be obtained in the absence of rGO/SnS_2,[31,32] which suggests that the rGO/SnS_2 composite favors the heterogeneous deposition of TEG on its surface. After reaction for 30 min, the resultant precipitates were collected by centrifugation and washed with ethanol 3 times. The dried precipitates were then dispersed in 100 mL deionized water and heated at 95 °C for 12 h. During this hydrothermal process, the TEG was converted into TiO_2 nanoparticles,[33] and the ternary rGO/SnS_2/TiO_2 composite was readily obtained. The resulting ternary composite was washed with deionized water 3 times and finally dried at 60 °C for 8 h in air.

Material characterization

The as-prepared samples were characterized *via* X-ray diffraction (XRD) on a Bruker diffractometer with Cu Kα radiation (λ = 0.15405 nm). The morphologies of the samples were observed with a field-emission scanning electron microscope (FESEM, Philips XL30). Transmission electron microscopy (TEM) images were acquired on a JEOL 2100F electron microscope operated at 200 kV. The surface elemental states of the samples were detected using X-ray photoelectron spectroscopy (XPS, Thermo Fisher, Alpha). The binding energy (BE) for the samples was calibrated using the C 1s peak from carbon tape at 284.8 eV. Thermogravimetric analysis (TGA) and differential scanning calorimetry (DSC) were performed in air using a Labsys EvoS60/58458 analyzer to determine the contents of SnS_2 and TiO_2 in the composites. The Brunner–Emmett–Teller (BET) specific surface area and Barrett–Joyner–Halenda (BJH) pore size distribution were determined through N_2 adsorption/desorption isotherms at 77 K on a Tri Star II 3020 surface area and porosity analyzer. Prior to sorption experiments, the samples were degassed at 100 °C for 48 h under vacuum. Raman measurements were recorded on a Nexus FTIR spectrometer using a 1064 nm laser.

Electrochemical measurements

The active materials (rGO/SnS_2 or rGO/SnS_2/TiO_2) were thoroughly mixed with acetylene black and polyvinylidene fluoride (PVDF) in a weight ratio of 8 : 1 : 1 to form a slurry with *N*-methyl-2-pyrrolidone (NMP) as the solvent. The slurry was pasted onto Cu foil which was dried at 110 °C under vacuum overnight. The mass loading was *ca.* 1 mg cm^{-2} for each electrode. CR2032-type coin cells were assembled in an Ar-filled glovebox with Li metal as the counter and reference electrodes. The electrolyte was a solution of 1 M $LiPF_6$ in ethylene carbonate and dimethyl carbonate (1 : 1 in volume ratio). Cyclic voltammetry (CV) was performed on a CHI 604e electrochemical workstation. Galvanostatic charge–discharge tests were performed on a LAND CT2001A battery tester in the voltage range of 3.0–0.05 V *vs.* Li^+/Li. The specific capacities of rGO/SnS_2 and rGO/SnS_2/TiO_2 were calculated based on the total weight of the composites for convenience. Electrochemical impedance spectroscopy (EIS) was performed on an electrochemical workstation (Autolab PGSTAT302N) in the frequency range of 100 kHz to 0.1 Hz at an amplitude of 10 mV. Prior to the EIS test, the Li-half cells were galvanostatic discharge–charge cycled at 50 mA g^{-1} for 3 cycles. All electrochemical tests were performed at room temperature.

Results and discussion

Fig. 1a depicts the XRD patterns of the binary rGO/SnS_2 and ternary rGO/SnS_2/TiO_2 nanocomposites. The two reflections observed in both patterns can be readily indexed to hexagonal SnS_2 with the space group $P\bar{3}m1$ (JCPDS card no. 23-0677).[25,34] The lack of some reflections suggest the low crystallinity and possible existence of defects in the SnS_2 product. In addition, the low-intensity, broadened (001) peak suggests the formation of small SnS_2 nanoparticles. The mean crystallite size was calculated to be ~3 nm along the [001] direction (*c*-axis) according to the Scherrer equation based on the full width at half maximum (FWHM) of the (001) plane, which corresponds to ~5 layers of stacking.[35] The few-layered SnS_2 may be beneficial for electrochemical Li storage due to the increased active sites for fast Li^+ insertion/extraction, favoured phase transition and shortened path for Li^+ diffusion. In addition, the bump centred at ~25.3° corresponds to the reflection from the few-layered rGO nanosheets.[23,24] In the rGO/SnS_2/TiO_2 sample, no reflections are observed for the TiO_2 phase, which suggests its relatively low content and uniform distribution on the rGO surface. The Raman spectra of rGO/SnS_2 and rGO/SnS_2/TiO_2 are shown in Fig. 1b. The two bands at ~1346.6 and 1609 cm^{-1} correspond to the disordered (D) band of sp^3-hybridized carbon and graphitic (G) band of sp^2-bonded carbon in graphite, respectively.[18] The intensity ratio of the D-band and G-band (I_D/

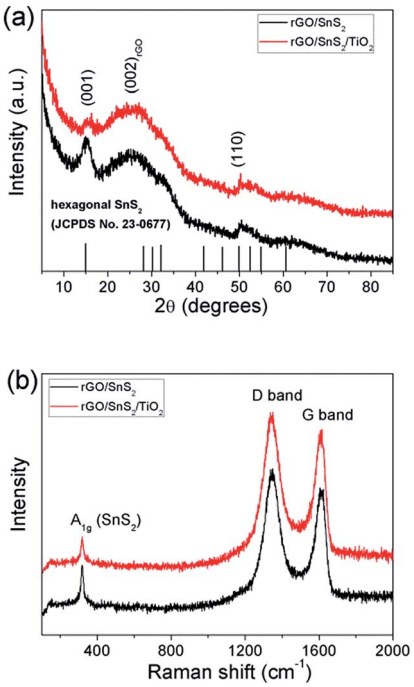

Fig. 1 (a) XRD patterns and (b) Raman spectra of the rGO/SnS_2 and rGO/SnS_2/TiO_2 samples.

I_G) in rGO/SnS_2 is ~1.17, which suggests the variation in the graphite plane structure triggered by the partial removal of oxygen-containing functional groups.[25] In addition, the weak band at ~316.8 cm^{-1} can be attributed to the out-of-plane Sn–S stretch vibration (A_{1g} mode) in SnS_2 with preferential edge-terminated sites and few-layer characteristics.[25,35,36] It should be noted that the E_{1g} mode (in-plane stretch vibration) is absent, possibly due to choice principle for scattering geometry in SnS_2 nanocrystals. This result indicates the successful deposition of ultrafine SnS_2 nanocrystals on the rGO surface. No Raman peaks were noted for TiO_2, which confirms its relatively low content and uniform distribution in the ternary heterostructure composite. TGA was further conducted to estimate the SnS_2 and TiO_2 contents in the composite materials (Fig. S1†). After heating in air, SnS_2 and rGO were converted into SnO_2 by oxidation/decomposition. The SnS_2 content in the binary rGO/SnS_2 composite was about 86 wt%, whereas for the ternary rGO/SnS_2/TiO_2, the contents of SnS_2 and TiO_2 were estimated to be *ca.* 74 wt% and 14 wt%, respectively.

The surface electronic states of the elements in the composites were studied by XPS. For the rGO/SnS_2 sample, its high-resolution C 1s XPS spectrum (Fig. S2a†) can be fitted into five species. The band at 284.7 eV is related to the sp^2-hybridized carbon in the graphene lattice. The band at 285.6 eV indicates the presence of C–N/C–S bonds in the composite.[13,27] The C–N bonding was introduced by *in situ* N-doping by EDA during the hydrothermal reduction of GO.[27] The N-doping is supposed to help stabilize SnS_2 during electrochemical cycling by N–Sn chemical interaction.[27] The formation of C–S bonds suggests interfacial coupling between SnS_2 and rGO,[37] which leads to enhanced charge transfer capability at the rGO/SnS_2 interface. The three remaining minor bands are attributed to C–O (286.6 eV), C=O (287.6 eV) and O–C=O (288.9 eV) induced by residual oxygen-functional groups on the rGO surface.[3] The deconvolution of the N 1s spectrum in Fig. S2b† reveals the existence of pyridinic N (398.9 eV), pyrrolic N (400.3 eV) and amino N (401.6 eV). The relatively weak intensity of the N 1s spectrum suggests a low N-doping content. Thus, N-doping alone is insufficient to fully anchor all the SnS_2 strongly on rGO. Thus, an extra surface coating is necessary to better stabilize the active SnS_2 species during cycling. In the S 2p spectrum (Fig. S2c†), the two major peaks at 163.2 and 162 eV can be indexed to S–Sn bonds. In addition, the two minor peaks located at 164.6 and 163.4 eV confirm the presence of S–C covalent bonds.[38] The Sn 3d XPS spectra in Fig. 2a disclose two sets of bands in both samples. For the rGO/SnS_2 sample, the bands centred at 495.7 and 487.3 eV with a spin-orbital splitting energy of 8.4 eV can be assigned to the $3d_{3/2}$ and $3d_{5/2}$ of Sn^{4+} ions in SnS_2, respectively.[39] The two minor peaks observed at 496.6 and 488.2 eV can be attributed to the small amount of SnO_2 species formed by surface oxidation.[40] No Sn–C bonds are detected *via* XPS, which is in agreement with recent literature.[41] In the rGO/SnS_2/TiO_2 composite, the two main peaks for Sn^{4+} in SnS_2 are centred at 495.6 and 487.2 eV, while the two minor peaks for SnO_2 are located at 496.5 and 488.1 eV. Compared to the rGO/SnS_2 sample, the Sn 3d peaks in rGO/SnS_2/TiO_2 show a slight shift toward the lower energy region, which suggests an increase in electron cloud density around SnS_2. Also, the Ti 2p peaks for Ti^{4+} in TiO_2 are observed at 465.2 eV (Ti $2p_{1/2}$) and 459.5 eV (Ti $2p_{3/2}$) (Fig. 2b), which shift to the higher energy region.[3] The shifts in BEs toward higher values for the Ti 2p

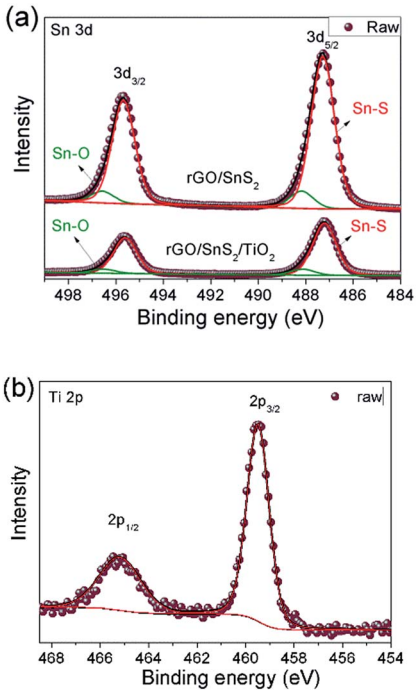

Fig. 2 High resolution XPS spectra of (a) Sn 3d and (b) Ti 2p in the rGO/SnS_2 and rGO/SnS_2/TiO_2 samples.

region and lower values for the Sn 3d region suggest that electrons transfer from TiO_2 to SnS_2 due to the lower Fermi energy level of SnS_2 caused by the larger Pauling electronegativity of Sn relative to Ti and more covalent character of the Sn–S bond than more ionic Ti–O bond. The XPS result indicates that an n–n type heterojunction forms at the SnS_2/TiO_2 interface with electron-enriched and depleted space-charge zones. The formation of nanoscale heterojunctions can enhance the rate property by boosting the charge transfer at the SnS_2/TiO_2 interface and Li^+ intercalation into the SnS_2 lattice.

The surface functional groups of the composites were further studied *via* FTIR spectroscopy. As shown in Fig. S3,† the bands at 3427 and 1577 cm^{-1} are ascribed to the –OH groups of adsorbed water molecules on the sample and the C=C vibration of the graphene lattice, respectively.[35] The band at ~1182 cm^{-1} is related to the C–O functional group on the rGO surface.[35,42] The bands at 1042 cm^{-1} and 876 cm^{-1} with low intensity correspond to the stretching vibration and bending vibration of the C–N bond,[43] respectively, which suggest low-concentration N-doping in the graphene lattice. This result is consistent with the above XPS result (Fig. S2†). In addition, the broad band centred at ~616 cm^{-1} represents the Sn–S bond stretching in rGO/SnS_2.[42] The combined XPS and FTIR results suggest the successful growth of SnS_2 and TiO_2 on the rGO nanosheets.

The surface morphology, particle size and microstructure of the samples were observed *via* SEM, TEM and HRTEM. SEM and TEM (Fig. S4†) reveal the sheet-like morphology of the resultant rGO/SnS_2 composite with a coarse and corrugated surface, and many SnS_2 nanoparticles uniformly and densely deposited on the rGO nanosheets. The uniform deposition of SnS_2 particles on the rGO nanosheets prevents the self-aggregation of both components. After TiO_2 coating, the morphology of the $rGO/SnS_2/TiO_2$ sample resembles that of its rGO/SnS_2 counterpart, which suggests the uniform deposition of TiO_2 surrounding the SnS_2 nanocrystals. Both the SEM and TEM images (Fig. 3a and b) suggest few-layered characteristics for the rGO nanosheets.

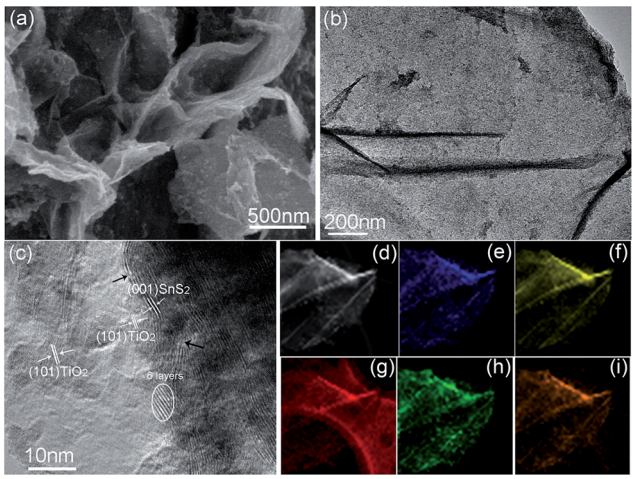

Fig. 3 (a) SEM and (b) TEM images. (c) HRTEM micrograph and (d) STEM-HAADF image and EDX mapping of (e) Sn, (f) S, (g) C, (h) Ti, and (i) O elements in the $rGO/SnS_2/TiO_2$ composite.

The TEM micrograph further reveals a dense array of ultrafine SnS_2/TiO_2 nanoparticles were anchored on the surface of the rGO nanosheets. The size of SnS_2 is rather small (~10 nm). The absence of large aggregates of discrete rGO or SnS_2 implies the controlled heterogeneous nucleation and growth of SnS_2 nanocrystals on the rGO substrate. Also, no discrete SnS_2 or TiO_2 nanoparticles are found by intensive TEM observation, which indicates the successful fabrication of the 2D rGO-based nanosheet composite and no detachment of SnS_2/TiO_2 from the rGO nanosheets during the ultrasonic treatment for TEM sample preparation. This result suggests that both SnS_2 and TiO_2 are tightly anchored on rGO which is possibly due to the formation of S–C/N–Sn bonds in the rGO/SnS_2 and SnS_2/TiO_2 junctions, as revealed by the XPS analysis (Fig. 2 and S2†). In the HRTEM micrograph (Fig. 3c), most of the SnS_2 exhibit a plate-like morphology and most of the plates align with their *c*-axis ([001] direction) normal to the rGO nanosheets, exposing their (001) planes. Some disconnections of the lattice fringes can also be observed, which indicate the presence of some dislocations (see arrows). The co-existence of exposed (001) facets and structural defects can be beneficial for facile Li^+ insertion and excess storage as well as structural phase transitions upon Li^+ intercalation. From some standing SnS_2 plates, the thickness of the plates is estimated to be less than 8 nm, which corresponds to a maximum of ~10 layers of stacking and agrees with the XRD result (Fig. 1a). The lateral size of the plates is under 10 nm. In addition, the clear lattice fringes with interplanar distances of 0.35 nm can be indexed to the (101) crystal plane of anatase TiO_2 crystallites. Furthermore, the SnS_2 and TiO_2 nanocrystals intimately contact during their heterogeneous deposition on the rGO substrate in sequence. Scanning transmission electron microscopy-energy disperse spectroscopy (STEM-EDS) elemental mapping (Fig. 3d–i) further confirms the uniform distribution of SnS_2 and TiO_2 on the rGO nanosheets, which suggests the formation of abundant SnS_2/TiO_2 heterojunctions. These nanoscale heterostructures with a built-in electric field can boost the Li^+/e^- transport/transfer at the SnS_2/TiO_2 interfaces during charge/discharge, rendering a higher rate capacity. The few-layered $rGO/SnS_2/TiO_2$ composite with anti-aggregation characteristics is also endowed with a high specific surface area of 117 $m^2\ g^{-1}$, as determined from the N_2 adsorption/desorption isotherms measured at 77 K.

The electrochemical properties of the as-prepared composite electrode materials were evaluated using coin-type Li-half cells. SnS_2 undergoes a lithiation/delithiation process *via* the following reactions:

$$SnS_2 + 4Li^+ + 4e^- \rightarrow Sn + 2Li_2S \quad (1)$$

$$Sn + 4.4Li^+ + 4.4e^- \rightarrow Li_{4.4}Sn \quad (2)$$

The conversion reaction (1) is generally considered to be less reversible, whereas the alloy reaction (2) is highly reversible, providing a theoretical capacity of ~645.6 mA h g^{-1}.[44] Fig. 4a presents the CV curves for first four cycles of the as-prepared $rGO/SnS_2/TiO_2$ electrode at the scan rate of 0.2 mV s^{-1}. During the first cathodic scan, the peak at ~1.5 V corresponds

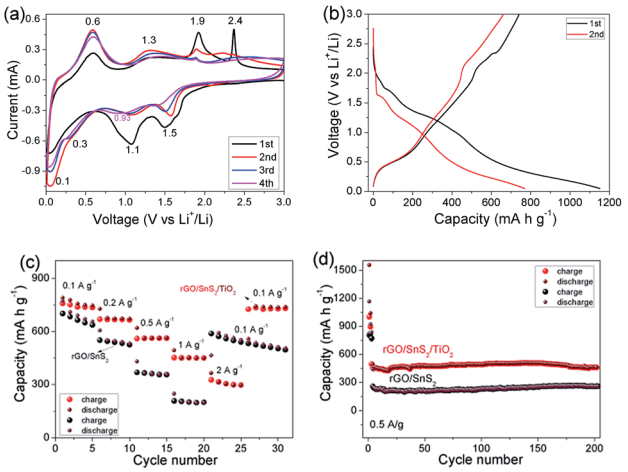

Fig. 4 Electrochemical properties of the rGO/SnS_2 and rGO/SnS_2/TiO_2 composite electrodes. (a) CV of rGO/SnS_2/TiO_2 recorded at 0.2 mV s^{-1}, (b) first and second galvanostatic charge/discharge curves of rGO/SnS_2/TiO_2 at 50 mA g^{-1}, (c) rate and (d) cycling properties of the rGO/SnS_2 and rGO/SnS_2/TiO_2 composite electrodes.

to Li^+ intercalation into the SnS_2 lattice with the formation of Li_xSnS_2 solid solutions[45] as well as the lithiation of TiO_2.[30] The partial lithiation of TiO_2 may afford some excess capacity contribution to the ternary rGO/SnS_2/TiO_2 composite. The reduction peak at ~1.1 V can be assigned to the decomposition of SnS_2 nanoparticles into metallic Sn and Li_2S as well as the formation of a solid-electrolyte interphase (SEI) layer.[45] The appearance of another reduction peak between 0.3 and 0.1 V suggests the formation of Li_xSn alloys.[44] In the following anodic scan, the peaks at ~0.6 V, 1.3 V and 1.9 V correspond to the reversible re-oxidation of Li_xSn to Sn, oxidation of part Sn into SnS_2, and deintercalation of Li^+ from TiO_2, respectively. The gradual increase in peak intensity at 0.6 V indicates an activation process in the composite electrode. The weak oxidation peak at 1.3 V implies reaction (1) is partly reversible in our experiment due to the small particle size of SnS_2 and its electrical wiring with rGO as well as the conformal TiO_2 coating which limits its aggregation and detachment from the rGO substrate. In addition, another oxidation peak is noted at ~2.4 V in the first anodic process, which is due to the oxidation of trace Li_2S into element S. Fig. 4b shows the first and second galvanostatic discharge/charge curves of the rGO/SnS_2/TiO_2 composite electrode at 50 mA g^{-1}. Similarly, several plateaus can be observed in the discharge and charge curves, which is in good agreement with the CV curves in Fig. 4a. The composite electrode has high initial discharge and charge capacities of 1152 and 740.6 mA h g^{-1}, with a coulombic efficiency (CE) of 64.3%, respectively. The large initial irreversible capacity loss is mainly ascribed to the decomposition of electrolyte and formation of an SEI film, as well as the lower reversibility of the conversion reaction (1). In the second cycle, the composite exhibits discharge and charge capacities of 770.7 and 661 mA h g^{-1}, respectively, with a much-improved CE value of 85.8%. As shown in Fig. 4c, the rGO/SnS_2/TiO_2 composite exhibits good rate capability, displaying stable capacities of 747, 667, 563, 454 and 303 mA h g^{-1} at current densities of 0.1, 0.2, 0.5, 1 and 2 A g^{-1}, respectively. A reversible capacity of 729 mA h g^{-1} can be recovered after suddenly switching the current density to 0.1 A g^{-1} again. In comparison, the rGO/SnS_2 composite electrode manifests an inferior lithium storage property with lower capacities of 667, 542, 365 and 205 mA h g^{-1} at 0.1, 0.2, 0.5 and 1 A g^{-1}, respectively. After decreasing the current density to 0.1 A g^{-1}, the material has a capacity of 576 mA h g^{-1}. To discern the possible capacity contribution of the rGO substrate, the electrochemical property of a pure rGO nanosheet electrode in Li-half cells was also evaluated. As shown in Fig. S5,† the pure rGO electrode displays a reversible Li^+ ion storage capacity of ~95 mA h g^{-1} at 1 A g^{-1}. Thus, its contribution to the overall capacity in both rGO/SnS_2 and rGO/SnS_2/TiO_2 is insignificant considering its relatively low mass content (14 wt% in rGO/SnS_2 and 12 wt% in rGO/SnS_2/TiO_2). The long-term cycling property of the two electrodes was further studied as shown in Fig. 4d. The rGO/SnS_2/TiO_2 composite displays a high and stable capacity of 485 mA h g^{-1} after 200 cycles, which is more than twice that of the rGO/SnS_2 electrode. This capacity difference should be not attributed to the low content of SnS_2 in rGO/SnS_2/TiO_2 since the specific capacity was calculated based on the total weight of the composite. Fig. S6† presents the 200th galvanostatic charge/discharge curves of the two electrodes. A larger polarization is observed for the rGO/SnS_2 electrode during charge/discharge which is possibly due to its instability during long-term cycling. In contrast, enhanced reaction kinetics is observed for the rGO/SnS_2/TiO_2 electrode during charge/discharge because the decoration of TiO_2 improves the stability of SnS_2 and promotes the charge transfer kinetics at the SnS_2/TiO_2 interface. The morphologies of the two electrodes after cycling for 200 cycles were further studied *via ex situ* SEM, as shown in Fig. S7.† The low-magnification SEM image (Fig. S7a†) reveals that the rGO/SnS_2/TiO_2 electrode film remains flat with slight cracks formed after electrochemical cycling, which suggests its good structural integrity and stability during charge/discharge. However, the high-magnification SEM images of the rGO/SnS_2/TiO_2 and rGO/SnS_2 electrodes (Fig. S7b and c†) apparently seem similar and less information can be derived from them. This difficulty mainly stems from the presence of a moisture-sensitive, electronically-insulating SEI film totally covering both electrode surfaces, which tends to decompose under intensive SEM/TEM characterization at high acceleration voltages. The electrochemical performance of the ternary rGO/SnS_2/TiO_2 composite electrode also surpasses some literature results, such as ultrathin SnS_2 nanoparticles on rGO nanosheets (~400 mA h g^{-1} at 584 mA g^{-1})[15] and free-standing SnS_2 nanosheets on 3D rGO foam (569.6, 433.3 and 174.1 mA h g^{-1} at 0.5, 1 and 2 A g^{-1}, respectively).[46]

The electrode reaction kinetics were further studied *via* electrochemical impedance spectroscopy (EIS). Fig. 5 shows the Nyquist plots of the two electrodes and corresponding fitted curves with the Zview software using the equivalent circuit model shown in the inset. The Nyquist plots contain two depressed semicircles, which correspond to the surface film resistance (R_f) in the high frequency region and charge transfer resistance (R_{ct}) at the high-to-medium frequency region, as well

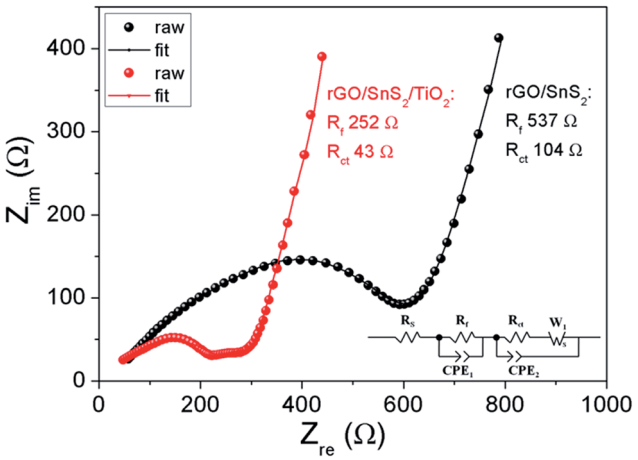

Fig. 5 Electrochemical impedance spectra (EIS) and equivalent electric circuit (inset) of the rGO/SnS_2 and rGO/SnS_2/TiO_2 electrodes.

as a sloping line related to Li^+ diffusion in the solid phase.[30,47] This reveals that the rGO/SnS_2/TiO_2 electrode has a smaller R_f (252 Ω) and R_{ct} (43 Ω) than that of the rGO/SnS_2 electrode (R_f of 537 Ω and R_{ct} of 104 Ω). This result suggests that the introduction of TiO_2 effectively improves the electrode/electrolyte interfacial characteristics by regulating the surface chemistry of SnS_2 and creating SnS_2/TiO_2 heterojunctions. In addition, the electron transport can be improved by the introduction of TiO_2. This can be explained by (1) the presence of abundant nanosized SnS_2/TiO_2 heterojunctions due to the interface charge transfer induced by their misaligned energy levels, as confirmed by TEM and XPS analyses. Such nanoscale junctions with a self-building interfacial electric field can drive e^- and Li^+ towards respective directions during discharge/charge, boosting the discharge capacity and rate property. (2) During the discharge/charge process, the partial lithiation of TiO_2 interparticles creates a continuous electron-permeable pathway for quick electron transport at the SnS_2 surface.

The superior electrochemical performance of the rGO/SnS_2/TiO_2 composite can be ascribed to the synergy of the 2D graphene nanosheets, ultrafine SnS_2 and TiO_2 nanoparticles as well as abundant nanoscale heterojunctions, as schematically shown in Scheme 2. (i) The rGO nanosheets feature high-speed electron transport. In addition, their high surface area improves the electrolyte permeation and diffusion, as well as affords an ideal host for the large-scale deposition of SnS_2 nanoparticles. (ii) The ultrafine SnS_2 particles with defects facilitate Li^+ intercalation and phase change during lithiation, as well as reduce the Li^+ diffusion path lengths. (iii) TiO_2 can possibly help to better physically anchor and separate SnS_2 nanocrystals during cycling, thus improving the structural stability during material synthesis and electrochemical cycling. (iv) The formed SnS_2/TiO_2 heterostructure with a self-building electric field can promote charge transfer at interface, as evidenced by the enhanced rate property and decreased charge transfer resistance in the EIS measurement.[3,48] (v) TiO_2 can afford trace extra capacity and enhance electron transport after partial lithiation.

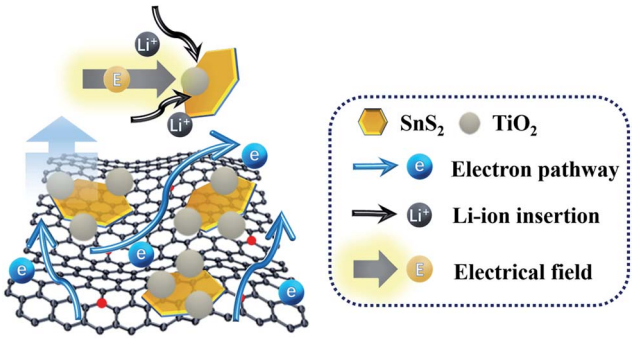

Scheme 2 Illustration of the structure characteristics of the ternary rGO/SnS_2/TiO_2 composite as an anode in LIBs.

Conclusions

A ternary rGO/SnS_2/TiO_2 heterostructured composite was designed and synthesized *via* a two-step solution process. The result composite is comprised of abundant few-layered rGO nanosheets decorated with few-layered ultrafine SnS_2 nanoparticles with defects. The SnS_2 particles were decorated with TiO_2 nanoparticles with intimate contact, forming nanoscale SnS_2/TiO_2 heterojunctions. This ternary rGO/SnS_2/TiO_2 composite exhibits superior electrochemical lithium storage capability due to the synergetic effects of its respective components with rapid electron/ion transport, reduced particle aggregation/detachment, as well as boosted charge transfer at SnS_2/TiO_2 heterointerfaces driven by a built-in electric field. This structure design can pave the way for the development of novel heterojunction-based composite materials for applications in lithium and post-lithium ion batteries.

Conflicts of interest

There are no conflicts to declare.

Acknowledgements

This work is supported by the National Natural Science Foundation of China (51302204) and National Science Foundation (DMR No. 1505902). Part of this work was conducted at the Molecular Analysis Facility, a National Nanotechnology Coordinated Infrastructure site at the Clean Energy Institute in University of Washington (Grant ECC-1542101). H. E. Wang acknowledges Hubei Provincial Department of Education for the "Chutian Scholar" program. H. E. Wang (No. 201506955047) and X. Zhao (No. 201506120144) are grateful for a scholarship from China Scholarship Council (CSC).

Notes and references

1 (*a*) Q. F. Zhang, S. L. Candelaria, E. Uchaker and G. Z. Cao, *Chem. Soc. Rev.*, 2013, **42**, 3127–3171; (*b*) C. F. Liu, Z. G. Neale and G. Z. Cao, *Mater. Today*, 2016, **19**, 109–123; (*c*) R. C. Masse, C. F. Liu, Y. W. Li, L. Q. Mai and G. Z. Cao, *Natl. Sci. Rev.*, 2017, **4**, 26–53.

2 (*a*) Y. Cai, H. E. Wang, S. Z. Huang, M. F. Yuen, H. H. Cai, C. Wang, Y. Yu, Y. Li, W. J. Zhang and B. L. Su, *Electrochim. Acta*, 2016, **210**, 206–214; (*b*) X. Zhao, H. E. Wang, J. Cao, W. Cai and J. Sui, *Chem. Commun.*, 2017, **53**, 10723–10726.
3 Y. Cai, H.-E. Wang, X. Zhao, F. Huang, C. Wang, Z. Deng, Y. Li, G. Cao and B.-L. Su, *ACS Appl. Mater. Interfaces*, 2017, **9**, 10652–10663.
4 M. N. Obrovac and V. L. Chevrier, *Chem. Rev.*, 2014, **114**, 11444–11502.
5 S. Z. Huang, Y. Cai, J. Jin, J. Liu, Y. Li, H. E. Wang, L. H. Chen, T. Hasan and B. L. Su, *J. Mater. Chem. A*, 2016, **4**, 4264–4272.
6 X. F. Zheng, H. E. Wang, C. Wang, Z. Deng, L. H. Chen, Y. Li, T. Hasan and B. L. Su, *Nano Energy*, 2016, **22**, 269–277.
7 H. E. Wang, L. J. Xi, R. G. Ma, Z. G. Lu, C. Y. Chung, I. Bello and J. A. Zapien, *J. Solid State Chem.*, 2012, **190**, 104–110.
8 Z. Q. Zhu, S. W. Wang, J. Du, Q. Jin, T. R. Zhang, F. Y. Cheng and J. Chen, *Nano Lett.*, 2014, **14**, 153–157.
9 B. Huang, X. H. Li, Y. Pei, S. Li, X. Cao, R. C. Masse and G. Z. Cao, *Small*, 2016, **12**, 1945–1955.
10 J. H. Kim, K. M. Jeon, J. S. Park and Y. C. Kang, *J. Power Sources*, 2017, **359**, 363–370.
11 B. Luo, Y. Fang, B. Wang, J. S. Zhou, H. H. Song and L. J. Zhi, *Energy Environ. Sci.*, 2012, **5**, 5226–5230.
12 T. F. Zhou, W. K. Pang, C. F. Zhang, J. P. Yang, Z. X. Chen, H. K. Liu and Z. P. Guo, *ACS Nano*, 2014, **8**, 8323–8333.
13 J. Sheng, L. Yang, Y. Zhu, F. Li, Y. Zhang and Z. Zhou, *J. Mater. Chem. A*, 2017, **5**, 19745–19751.
14 Y. Zhao, X. Li, B. Yan, D. Li, S. Lawes and X. Sun, *J. Power Sources*, 2015, **274**, 869–884.
15 M. Sathish, S. Mitani, T. Tomai and I. Honma, *J. Phys. Chem. C*, 2012, **116**, 12475–12481.
16 K. Y. Li, S. C. Yan, Z. X. Lin and Y. Shi, *J. Alloys Compd.*, 2016, **681**, 486–491.
17 K. X. Tu, F. Y. Li and Z. F. Chen, *J. Mater. Res.*, 2016, **31**, 878–885.
18 S. Liu, X. Lu, J. Xie, G. Cao, T. Zhu and X. Zhao, *ACS Appl. Mater. Interfaces*, 2013, **5**, 1588–1595.
19 Y. C. Liu, H. Y. Kang, L. F. Jiao, C. C. Chen, K. Z. Cao, Y. J. Wang and H. T. Yuan, *Nanoscale*, 2015, **7**, 1325–1332.
20 Q. Wu, L. F. Jiao, J. Du, J. Q. Yang, L. J. Guo, Y. C. Liu, Y. J. Wang and H. T. Yuan, *J. Power Sources*, 2013, **239**, 89–93.
21 J. P. Li, P. Wu, F. J. Lou, P. Zhang, Y. W. Tang, Y. M. Zhou and T. H. Lu, *Electrochim. Acta*, 2013, **111**, 862–868.
22 Y. R. Ren, J. W. Wang, X. B. Huang and J. N. Ding, *Mater. Lett.*, 2017, **186**, 57–61.
23 Y. D. Zhang, P. Y. Zhu, L. L. Huang, J. Xie, S. C. Zhang, G. S. Cao and X. B. Zhao, *Adv. Funct. Mater.*, 2015, **25**, 481–489.
24 K. Chang, Z. Wang, G. Huang, H. Li, W. Chen and J. Y. Lee, *J. Power Sources*, 2012, **201**, 259–266.
25 B. Luo, Y. Fang, B. Wang, J. Zhou, H. Song and L. Zhi, *Energy Environ. Sci.*, 2012, **5**, 5226–5230.
26 X. Zhou, L.-J. Wan and Y.-G. Guo, *Adv. Mater.*, 2013, **25**, 2152–2157.
27 (*a*) Y. Jiang, M. Wei, J. K. Feng, Y. C. Ma and S. L. Xiong, *Energy Environ. Sci.*, 2016, **9**, 1430–1438; (*b*) X. Zhao, H. E. Wang, R. C. Massé, J. Cao, J. Sui, J. Li, W. Cai and G. Z. Cao, *J. Mater. Chem. A*, 2017, **5**, 7394–7402.
28 J. Yang, Y. Wang, W. Li, L. Wang, Y. Fan, W. Jiang, W. Luo, Y. Wang, B. Kong, C. Selomulya, H. K. Liu, S. X. Dou and D. Zhao, *Adv. Mater.*, 2017, DOI: 10.1002/adma.201700523.
29 (*a*) D. N. Wang, J. L. Yang, J. Liu, X. F. Li, R. Y. Li, M. Cai, T. K. Sham and X. L. Sun, *J. Mater. Chem. A*, 2014, **2**, 2306–2312; (*b*) H. Kou, X. F. Li, H. Shan, L. L. Fan, B. Yan and D. J. Li, *J. Mater. Chem. A*, 2017, **5**, 17881–17888.
30 Y. Cai, H.-E. Wang, J. Jin, S.-Z. Huang, Y. Yu, Y. Li, S.-P. Feng and B.-L. Su, *Chem. Eng. J.*, 2015, **281**, 844–851.
31 H. E. Wang, L. X. Zheng, C. P. Liu, Y. K. Liu, C. Y. Luan, H. Cheng, Y. Y. Li, L. Martinu, J. A. Zapien and I. Bello, *J. Phys. Chem. C*, 2011, **115**, 10419–10425.
32 H. E. Wang, H. Cheng, C. P. Liu, X. Chen, Q. L. Jiang, Z. G. Lu, Y. Y. Li, C. Y. Chung, W. Y. Zhang, J. A. Zapien, L. Martinu and I. Bello, *J. Power Sources*, 2011, **196**, 6394–6399.
33 L. S. Zhong, J. S. Hu, L. J. Wan and W. G. Song, *Chem. Commun.*, 2008, 1184–1186.
34 Y. Jiang, Y. Feng, B. Xi, S. Kai, K. Mi, J. Feng, J. Zhang and S. Xiong, *J. Mater. Chem. A*, 2016, **4**, 10719–10726.
35 Y. Liu, H. Kang, L. Jiao, C. Chen, K. Cao, Y. Wang and H. Yuan, *Nanoscale*, 2015, **7**, 1325–1332.
36 Y. Q. Zhang, Z. L. Ma, D. D. Liu, S. Dou, J. M. Ma, M. Zhang, Z. P. Guo, R. Chen and S. Y. Wang, *J. Mater. Chem. A*, 2017, **5**, 512–518.
37 Z. L. Chen, R. B. Wu, M. Liu, H. Wang, H. B. Xu, Y. H. Guo, Y. Song, F. Fang, X. B. Yu and D. L. Sun, *Adv. Funct. Mater.*, 2017, **27**, 1702046.
38 X. Wang, G. Li, M. H. Seo, F. M. Hassan, M. A. Hoque and Z. Chen, *Adv. Energy Mater.*, 2015, **5**, 1501106.
39 D. H. Youn, S. K. Stauffer, P. Xiao, H. Park, Y. Nam, A. Dolocan, G. Henkelman, A. Heller and C. B. Mullins, *ACS Nano*, 2016, **10**, 10778–10788.
40 H. K. Wang, F. Fu, F. H. Zhang, H. E. Wang, S. V. Kershaw, J. Q. Xu, S. G. Sun and A. L. Rogach, *J. Mater. Chem.*, 2012, **22**, 2140–2148.
41 C. Gao, L. Li, A.-R. O. Raji, A. Kovalchuk, Z. Peng, H. Fei, Y. He, N. D. Kim, Q. Zhong, E. Xie and J. M. Tour, *ACS Appl. Mater. Interfaces*, 2015, **7**, 26549–26556.
42 S. Yan, K. Li, Z. Lin, H. Song, T. Jiang, J. Wu and Y. Shi, *RSC Adv.*, 2016, **6**, 32414–32421.
43 Z. Wu, Y. Xue, Y. Zhang, J. Li and T. Chen, *RSC Adv.*, 2015, **5**, 24640–24648.
44 X. Jiang, X. L. Yang, Y. H. Zhu, J. H. Shen, K. C. Fan and C. Z. Li, *J. Power Sources*, 2013, **237**, 178–186.
45 (*a*) L. Zhuo, Y. Wu, L. Wang, Y. Yu, X. Zhang and F. Zhao, *RSC Adv.*, 2012, **2**, 5084–5087; (*b*) L. Zhuo, Y. Wu, L. Wang, Y. Yu, X. Zhang and F. Zhao, *RSC Adv.*, 2012, **2**, 5084–5087; X. Zhao, H. E. Wang, X. Chen, J. Cao, Y. Zhao, Z. G. Neale, W. Cai, J. Sui and G. Z. Cao, *Energy Storage Materials*, 2018, **11**, 161–169.
46 Z. X. Huang, Y. Wang, J. I. Wong and H. Y. Yang, *2D Mater.*, 2015, **2**, 7.
47 (*a*) Z. X. Yu, X. F. Li, B. Yan, D. B. Xiong, M. Yang and D. J. Li, *Mater. Res. Bull.*, 2017, **96**, 516–532; (*b*) M. Yang, X. F. Li, B. Yan, L. L. Fan, Z. X. Yu and D. J. Li, *J. Alloys Compd.*, 2017, **710**, 323–330.
48 X. Zhao, J. Sui, F. Li, H. Fang, H. E. Wang, J. Li, W. Cai and G. Z. Cao, *Nanoscale*, 2016, **8**, 17902–17910.